Supporting Information for

Three-dimensional lead iodide perovskites based on complex ions

Hebin Wang,†[a] Yinye Yu,†[bcd] Haolin Lu,[a] Teng Wang,[a] Yuki Haruta,[e] Xingzhan Wei,[c] Guichuan Xing,[f] Makhsud I. Saidaminov,[g] Yecheng Zhou*[b] and Guankui Long*[a]

[a] *School of Materials Science and Engineering, National Institute for Advanced Materials, Renewable Energy Conversion and Storage Center (RECAST), Nankai University, 300350, Tianjin, China*

[b] *School of Materials Science and Engineering, Sun Yat-sen University, Guangzhou 510006, China*

[c] *Micro-nano Manufacturing and System Integration Center, Chongqing Institute of Green and Intelligent Technology, Chinese Academy of Sciences, Chongqing 400714, China*

[d] *University of Chinese Academy of Sciences, No. 19A Yuquan Road, Shijingshan District, Beijing 100049, China*

[e] *Department of Chemistry, University of Victoria, Victoria, British Columbia V8P 5C2, Canada*

[f] *Institute of Applied Physics and Materials Engineering, University of Macau, Avenida da Universidade, Taipa, Macau, 999078, China*

[g] *Department of Chemistry, Department of Electrical & Computer Engineering, and Centre for Advanced Materials and Related Technologies (CAMTEC), University of Victoria, Victoria, British Columbia V8P 5C2, Canada.*

** Corresponding author.*

† *These authors contributed equally to this work.*

Table of Contents

1. Methods

The Vienna *ab initio* simulation package (VASP)[1] software under the framework of density functional theory (DFT) is used to perform the calculations including *ab initio* molecular dynamics (AIMD)[2] simulations. The projector augmented-wave (PAW)[3] method is used to process the electrons near the nucleus, and the generalized gradient approximation (GGA) method of the Perdew-Burke-Ernzerh (PBE)[4] is used for the exchange correlation functional. The cutoff energy is set to 550 eV and 400 eV for structure relaxations and AIMD simulations, respectively. All structures are relaxed until the force on each atom is less than 0.001 eV/Å. Γ-centered 7×5×7 Monkhorst-Pack mesh K points are used in the static calculations of the proposed perovskites. The K points of 11×11×11 and 7×7×5 are used for the α- and β-phase $CH_3NH_3PbI_3$. For the electronic band structures calculations, 40 insertion K points between each pair of high symmetry points are used. Spin polarization is adopted for the calculation of DOS and band structures. The electronic structures of the proposed perovskites were also calculated by the Plane-Wave self-consistent field (PWscf) with PBE functional considering the spin-orbit coupling and the Scalar Relativistic (SR) effect.[5-6] While considering SR effect, the QUANTUM ESPRESSO was used.[7-8] Supercells with size of 17.0 Å × 25.3 Å × 18.4 Å for $Au(NH_3)_2PbI_3$, 17.1 Å × 25.2 Å × 18.4 Å for $Ag(NH_3)_2PbI_3$, and 17.3 Å × 25.1 Å × 18.5 Å for $Cu(NH_3)_2PbI_3$ at Γ point are used to perform AIMD simulations with a time step of 1 fs. The phonon spectra at 0 K were calculated by using Phonopy 2.15.[9-10] The calculation of phonon spectrum adopted Finite displacement method. Unit cells size used for calculations with 10.2 Å × 12.7 Å

× 8.8 Å for $Au(NH_3)_2PbI_3$, 10.1 Å × 12.6 Å × 8.9 Å for $Ag(NH_3)_2PbI_3$, and 9.8 Å × 12.7 Å × 8.7 Å for $Cu(NH_3)_2PbI_3$. The difference in iterative energy of electron density is less than 10^{-8} eV. The optical absorption spectrum is calculated based on a frequency-dependent dielectric function. The wave function of band structure was processed to obtain the optical transition between VB and CB by the VASPKIT code.[11]

2. Tolerance factor, formation energies and dissociation energies of 3D perovskites

Table S1. The calculated new tolerance factor of the proposed 3D perovskites with complex ion in this work and $FAPbI_3$.

	A_{eff}	B	X	τ_{au}
$Cu(NH_3)_2PbI_3$	3.34	1.19	2.20	3.57
$Ag(NH_3)_2PbI_3$	3.55	1.19	2.20	3.58
$Au(NH_3)_2PbI_3$	3.50	1.19	2.20	3.57
$FAPbI_3$	2.63	1.19	2.20	3.64

Table S2. The calculated formation energies and dissociation energies of the 3D perovskites with complex ions and $MAPbI_3$.

Materials	Formation energy (eV/atom)	Dissociation energy (eV/atom)
$Cu(NH_3)_2PbI_3$	-0.33	0.07
$Ag(NH_3)_2PbI_3$	-0.27	0.03
$Au(NH_3)_2PbI_3$	-0.24	0.06
$MAPbI_3$	-0.46	0.13

Table S3. The lattice constants of $Cu(NH_3)_2PbI_3$, $Ag(NH_3)_2PbI_3$ and $Au(NH_3)_2PbI_3$ after structure optimization.

Parameters	$Cu(NH_3)_2PbI_3$	$Ag(NH_3)_2PbI_3$	$Au(NH_3)_2PbI_3$
a/Å	9.8036	10.0749	10.2218
b/Å	12.6756	12.6159	12.6937
c/Å	8.7085	8.9010	8.7531
α/°	90.0001	89.9993	90.0000
β/°	90.0024	90.0395	90.0013
γ/°	90.0000	90.0015	90.0000
Unit cell volume/$Å^3$	1082.1809	1131.3692	1135.7576

3.The distortion of $Cu(NH_3)_2PbI_3$, $Ag(NH_3)_2PbI_3$ and $Au(NH_3)_2PbI_3$

The bond length distortion index (D) and bond angle variance (σ^2) were calculated based on Equation S1 and S2:

$$D = \frac{1}{6}\sum_{i=1}^{6}\frac{|d_i - d_0|}{d_0} \quad \text{(S1)}$$

$$\sigma^2 = \frac{1}{11}\sum_{i=1}^{12}(\theta_i - 90)^2 \quad \text{(S2)}$$

where d, d_0 and θ_i represent the Pb-I bond length, the mean Pb-I bond length and the angle of I-Pb-I bond of individual $[PbI_6]^{4-}$ octahedra, respectively.

Table S4. The distortion of $M(NH_3)_2PbI_3$ (M=Cu, Ag, Au) and γ-$MAPbI_3$.

Materials	D	σ^2	Pb-I-Pb angle (in-plane of (010))
$Cu(NH_3)_2PbI_3$	0.042	6.243	162.281
$Ag(NH_3)_2PbI_3$	0.047	11.464	159.821
$Au(NH_3)_2PbI_3$	0.031	22.504	163.260
γ-$MAPbI_3$	0.011	18.544	145.375

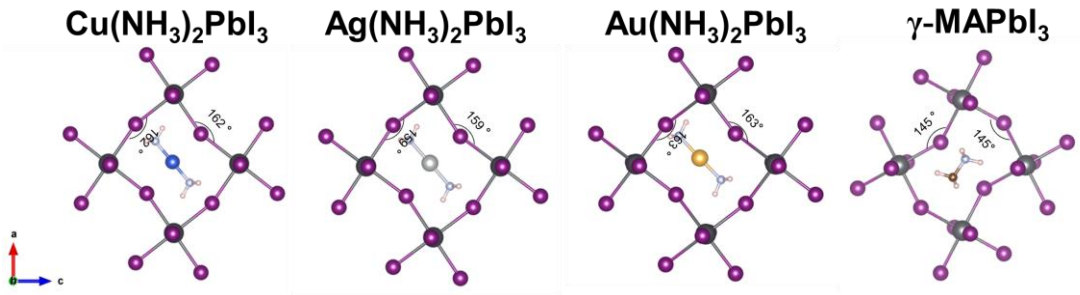

Figure S1. The angle of Pb-I-Pb bond (in-plane of (010)) in $M(NH_3)_2PbI_3$ (M=Cu, Ag, Au) and γ-$MAPbI_3$.

4. Vibration modes arising from the imaginary phonon frequencies

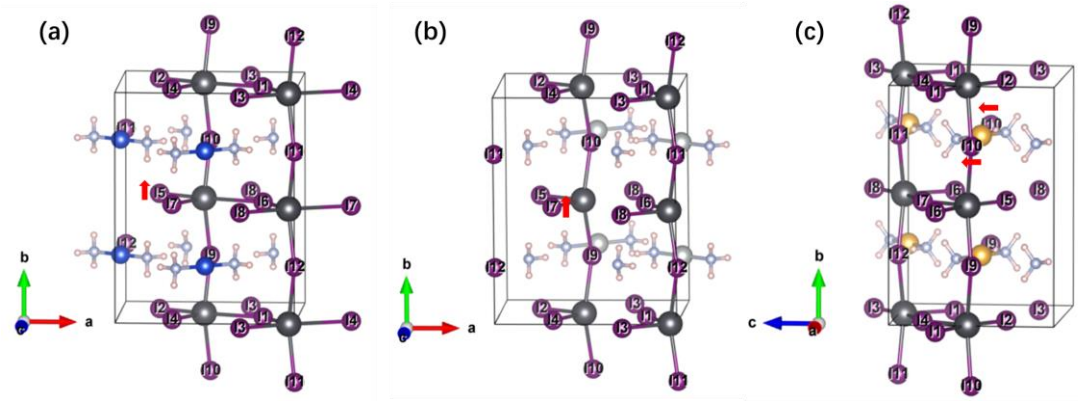

Figure S2. Vibration modes of $Cu(NH_3)_2PbI_3$ (a), $Ag(NH_3)_2PbI_3$ (b), and $Au(NH_3)_2PbI_3$ (c) arising from the imaginary phonon frequencies. The red arrows illustrate the vibration direction of the atom.

5. The effective masses of the 3D perovskites with complex ions

Table S5. The effective masses of the 3D perovskites with complex ions.

	Perovskite	$Cu(NH_3)_2PbI_3$							
	Direction	Γ-T	Γ-W	Γ-X	Harmonic mean	Γ-T	Γ-W	Γ-X	Harmonic mean
	Spin	up				down			
m_e*	CB3	0.25	0.25	4.11	0.66	0.25	0.25	4.06	0.66
	CB2	1.24	1.24	0.83		1.24	1.24	0.83	
	CB1	2.45	2.45	0.54		2.45	2.45	0.54	
	Harmonic mean	0.58	0.58	0.91		0.58	0.58	0.91	
	Direction	X-V	X-R	X-Γ		X-V	X-R	X-Γ	
m_h*	VB1	-20.03	-20.06	-20.99	-14.63	-20.03	-20.06	-20.99	-14.82
	VB2	-19.17	-19.20	-6.31		-20.20	-20.24	-6.31	
	Harmonic mean	-19.59	-19.62	-9.70		-20.11	-20.15	-9.70	
	Perovskite	$Ag(NH_3)_2PbI_3$							
	Direction	Γ-T	Γ-W	Γ-X		Γ-T	Γ-W	Γ-X	
	Spin	up				down			
m_e*	CB3	0.26	0.26	4.31	0.72	0.26	0.26	4.31	0.72
	CB2	1.99	2.00	4.03		1.99	2.00	4.03	
	CB1	2.61	2.61	0.38		2.61	2.61	0.38	
	Harmonic mean	0.63	0.63	0.96		0.63	0.63	0.96	
m_h*	VB1	-2.88	-2.89	-31.63	-4.14	-2.89	-2.89	-27.41	-4.12
	Perovskite	$Au(NH_3)_2PbI_3$							
	Direction	Γ-T	Γ-W	Γ-X		Γ-T	Γ-W	Γ-X	
	Spin	up				down			
m_e*	CB3	0.27	0.27	4.25	0.69	0.27	0.27	4.29	0.69
	CB2	1.02	1.02	4.55		1.02	1.02	4.55	
	CB1	2.23	2.24	0.42		2.23	2.24	0.42	
		0.58	0.58	1.06		0.58	0.58	1.06	
m_h*	VB1	-2.55	-2.55	-23.64	-3.63	-2.55	-2.55	-23.64	-3.63

6. The structures after ab initio molecular dynamics simulations

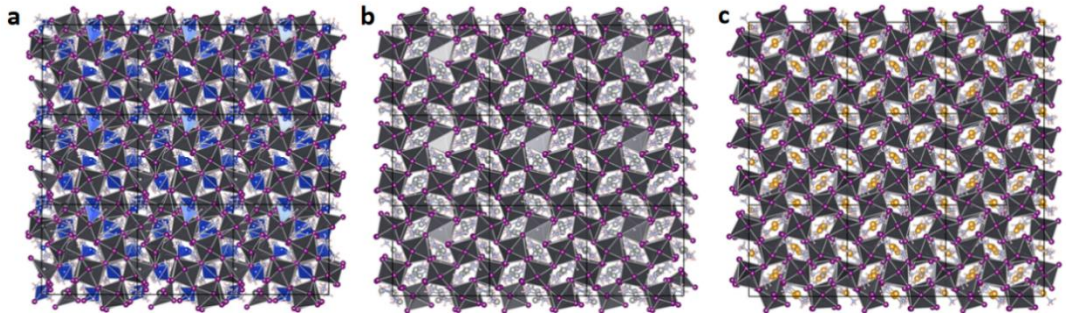

Figure S3. The 3×3 supercells of $Cu(NH_3)_2PbI_3$ (a), $Ag(NH_3)_2PbI_3$ (b), and $Au(NH_3)_2PbI_3$ (c) after *ab initio* molecular dynamics simulations (AIMD) with a total simulation time of 5 ps. The blue tetrahedron in (a) indicates the formation of Cu-I bond.

7. The calculated band structures of the 3D perovskite with complex ions

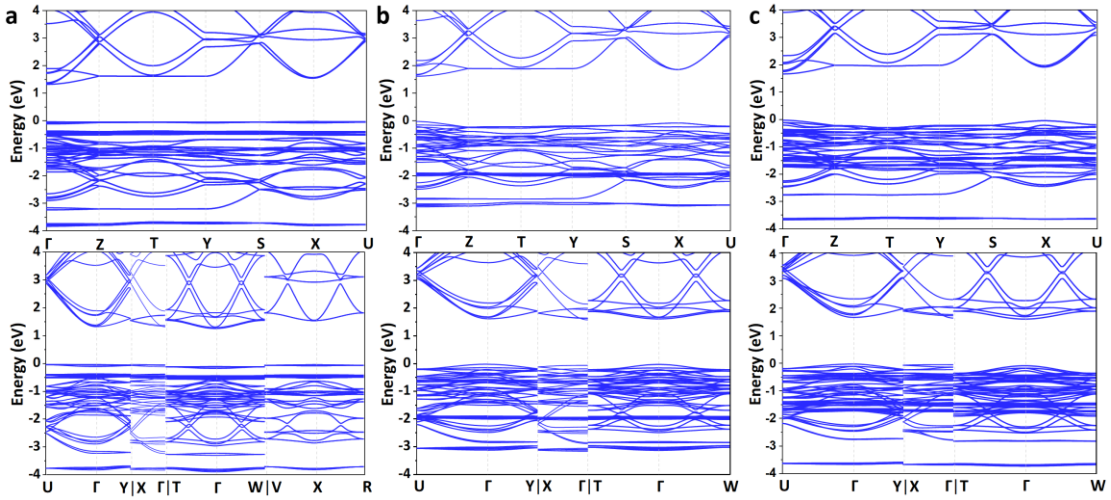

Figure S4. The calculated band structures of the 3D perovskite with complex ions based on the PBE functional: $Cu(NH_3)_2PbI_3$ (a), $Ag(NH_3)_2PbI_3$ (b), and $Au(NH_3)_2PbI_3$ (c).

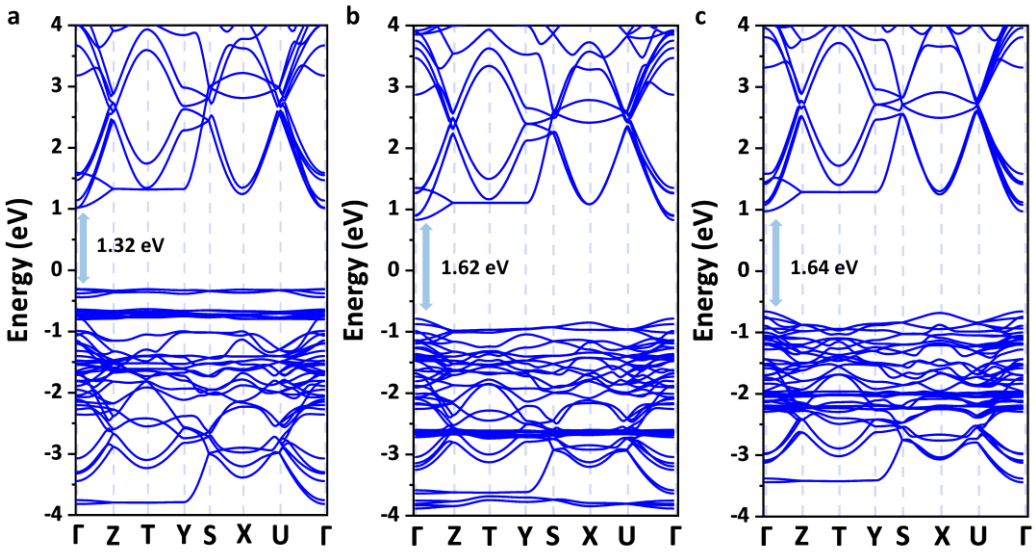

Figure S5. The calculated band structures of the 3D perovskite with complex ions based on the Plane-Wave self-consistent field (PWscf) with PBE functional considering the spin-orbit coupling and the Scalar Relativistic (SR) effect: $Cu(NH_3)_2PbI_3$ (a), $Ag(NH_3)_2PbI_3$ (b), and $Au(NH_3)_2PbI_3$ (c).

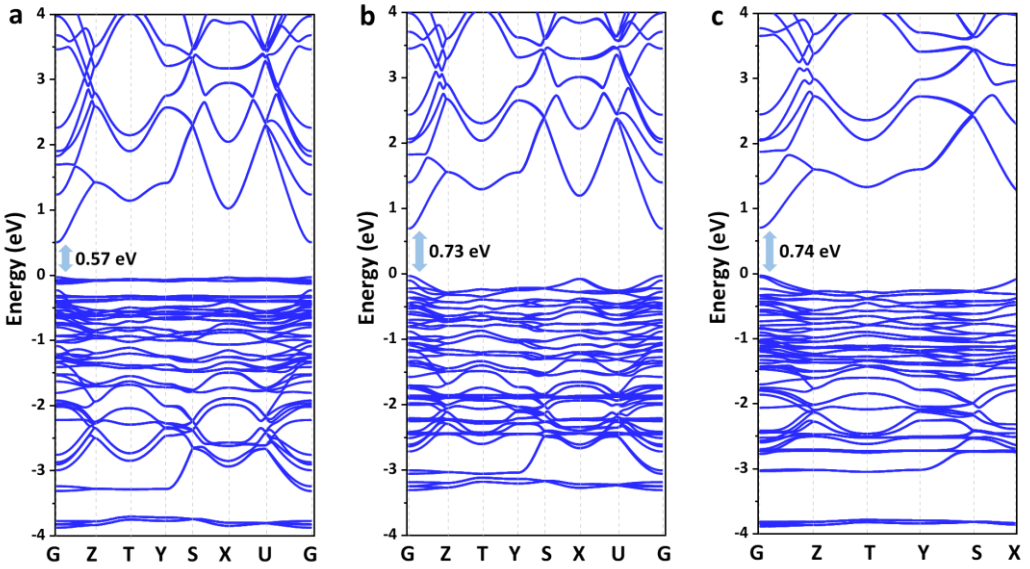

Figure S6. The calculated band structures of the 3D perovskite with complex ions based on the PBE functional considering spin-orbit coupling: $Cu(NH_3)_2PbI_3$ (a), $Ag(NH_3)_2PbI_3$ (b), and $Au(NH_3)_2PbI_3$ (c).

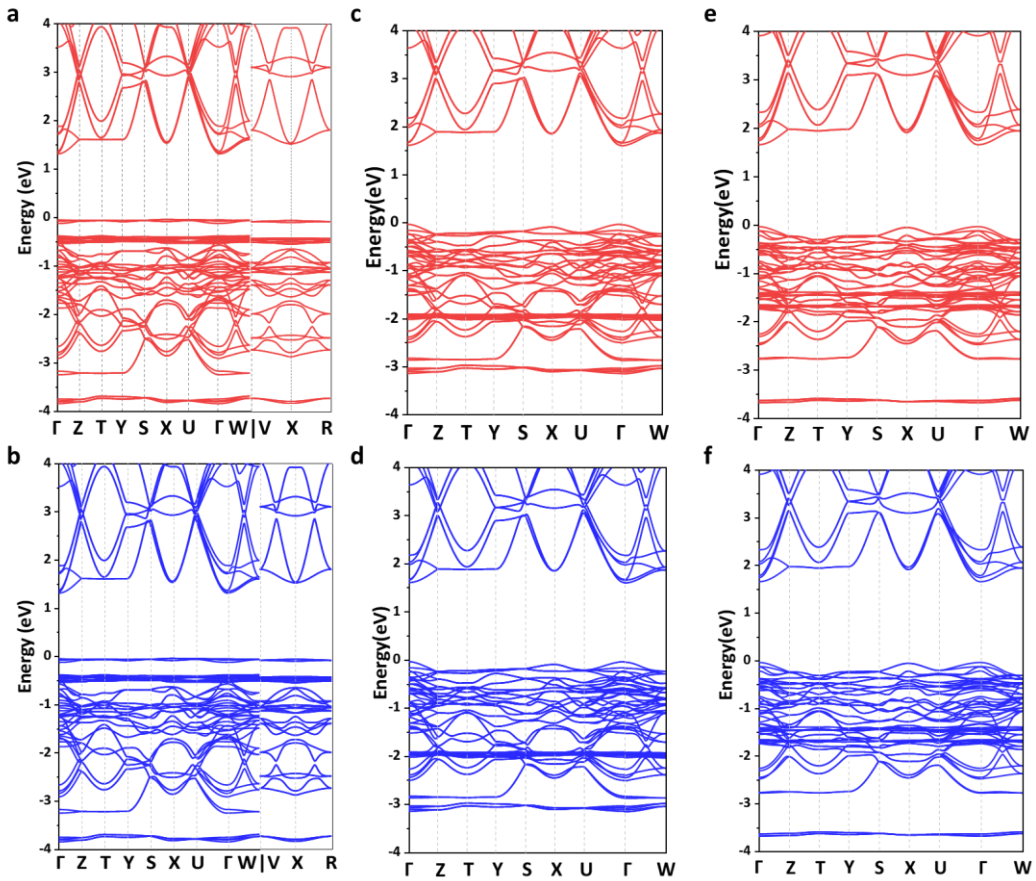

Figure S7. The calculated band structures of the 3D perovskite with complex ions considering the

electron spin: spin-up (a) and spin-down (b) for $Cu(NH_3)_2PbI_3$, spin-up (c) and spin-down (d) for $Ag(NH_3)_2PbI_3$ and spin-up (e) and spin-down (f) for $Au(NH_3)_2PbI_3$.

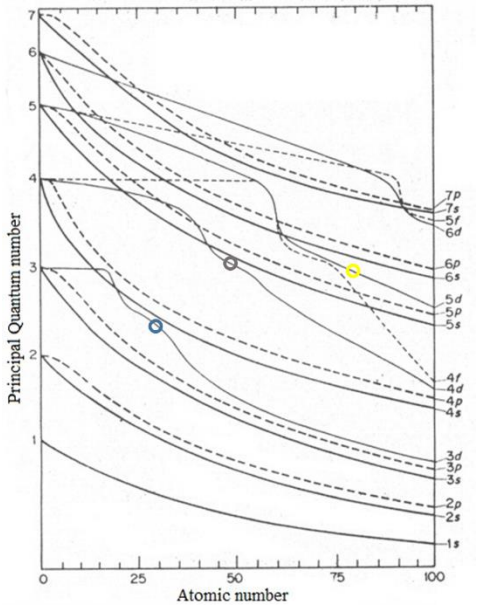

Figure S8. The energy level of different atomic orbits with increasing the atomic number. The blue, grey and yellow cycle represent the Cu 3*d*, Ag 4*d* and Au 5*d* orbit, respectively.[12]

8. The calculated optical properties of the 3D perovskite with complex ions and $MAPbI_3$

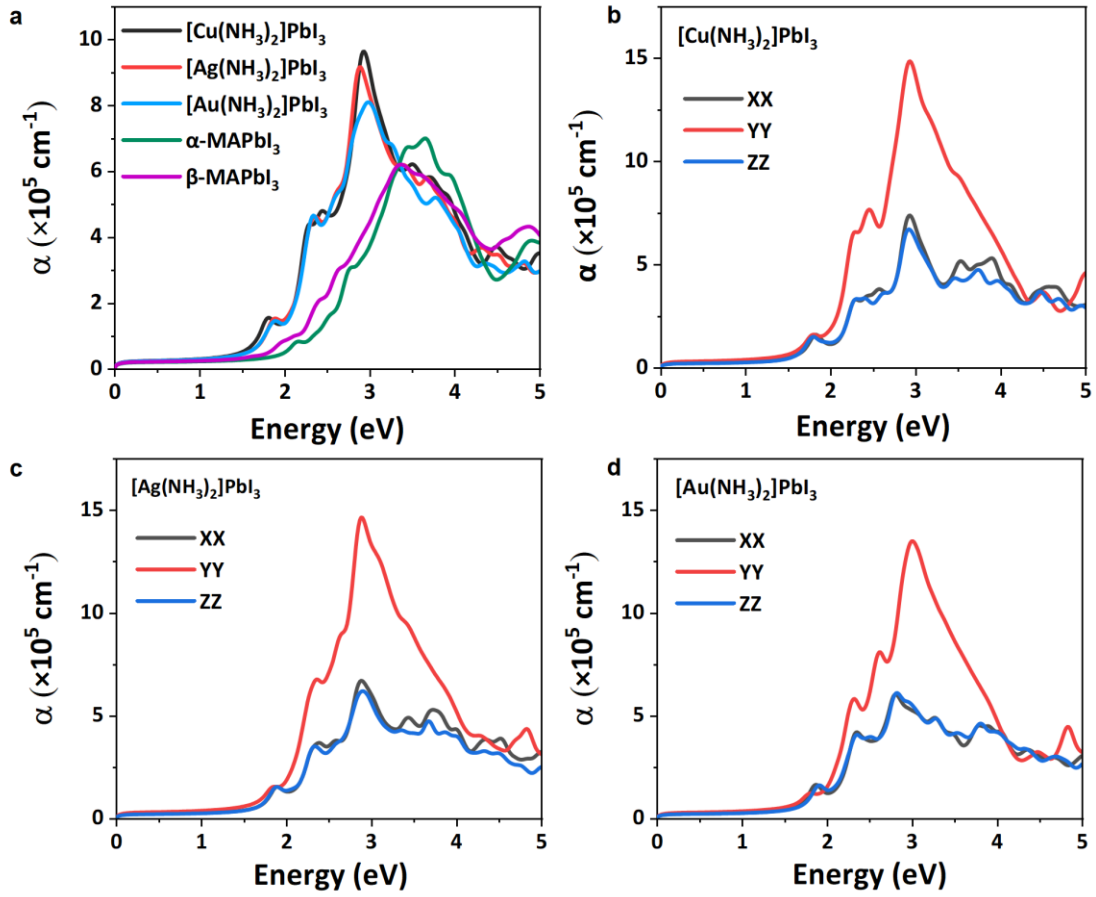

Figure S9. (a) Comparison of the calculated absorption spectra of the proposed perovskites with $CH_3NH_3PbI_3$. The calculated absorption spectra of $Cu(NH_3)_2PbI_3$ (b), $Ag(NH_3)_2PbI_3$ (c), and $Au(NH_3)_2PbI_3$ (d).

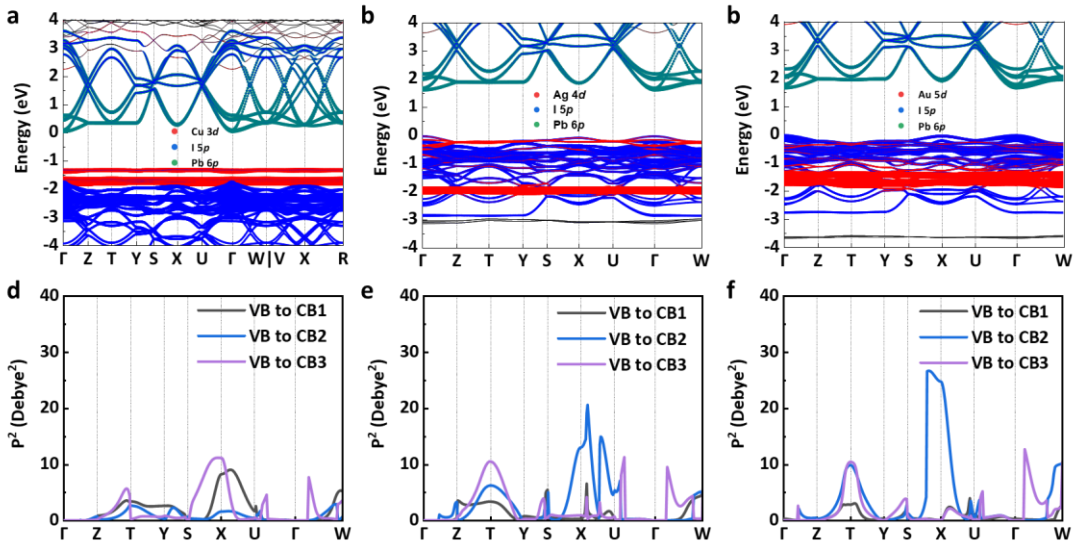

Figure S10. The calculated band structures of the 3D perovskite with complex ions: $Cu(NH_3)_2PbI_3$ (a), $Ag(NH_3)_2PbI_3$ (b), and $Au(NH_3)_2PbI_3$ (c). The square of the transition dipole moment from VB to CB of $Cu(NH_3)_2PbI_3$ (d), $Ag(NH_3)_2PbI_3$ (e), and $Au(NH_3)_2PbI_3$ (f).

9. The calculated projected density of states (PDOS) of the 3D perovskite with complex ions

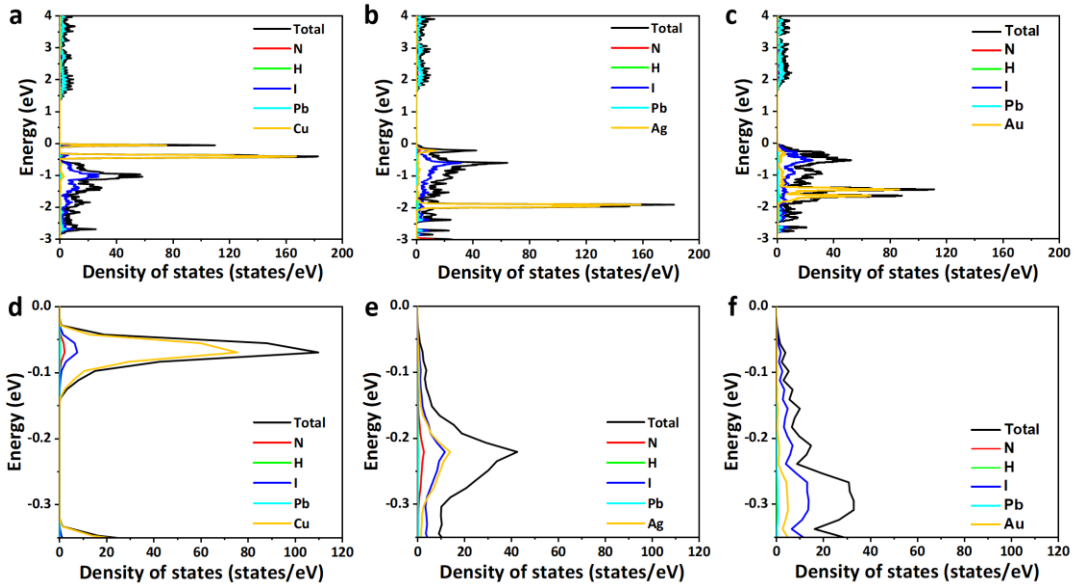

Figure S11. The calculated projected density of states (PDOS) of the 3D perovskite with complex ions based on the PBE functional: $Cu(NH_3)_2PbI_3$ (a), $Ag(NH_3)_2PbI_3$ (b), and $Au(NH_3)_2PbI_3$ (c). The magnified PDOS at VBM of $Cu(NH_3)_2PbI_3$ (d), $Ag(NH_3)_2PbI_3$ (e) and $Au(NH_3)_2PbI_3$ (f).

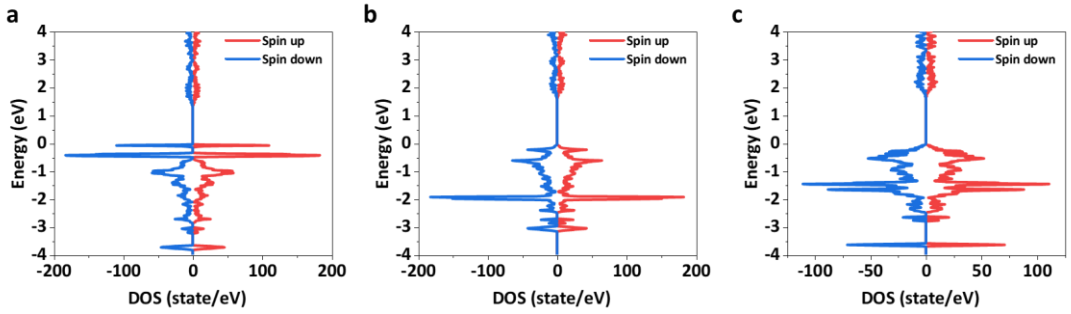

Figure S12. The calculated projected density of states (PDOS) of the 3D perovskite with complex ions considering the electron spin: $Cu(NH_3)_2PbI_3$ (a), $Ag(NH_3)_2PbI_3$ (b), and $Au(NH_3)_2PbI_3$ (c).

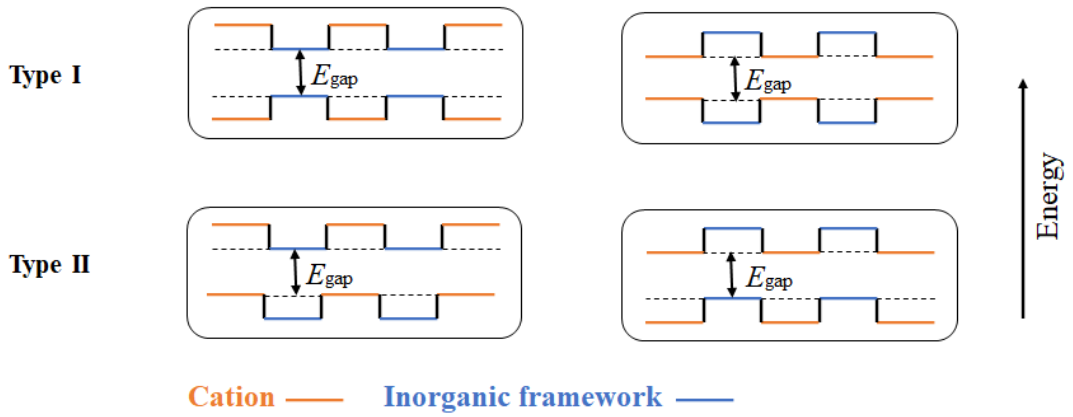

Figure S13. The possible energy level alignments for the alternating organic-inorganic hybrid halide perovskites containing organic/inorganic cations are shown, with arrows and dashed lines indicating the overall bandgap.

10. The electron density of the CBM or VBM of the 3D perovskite with complex ions

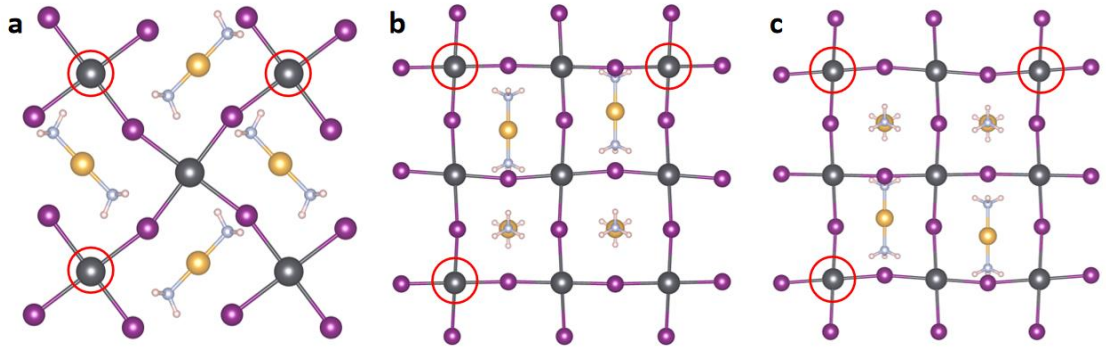

Figure S14. The plane used in the 2D electron density of $Au(NH_3)_2PbI_3$. (010) (a), (101) (b), (10$\bar{1}$) (c). The atoms used while slicing thee planes were labelled using red circles.

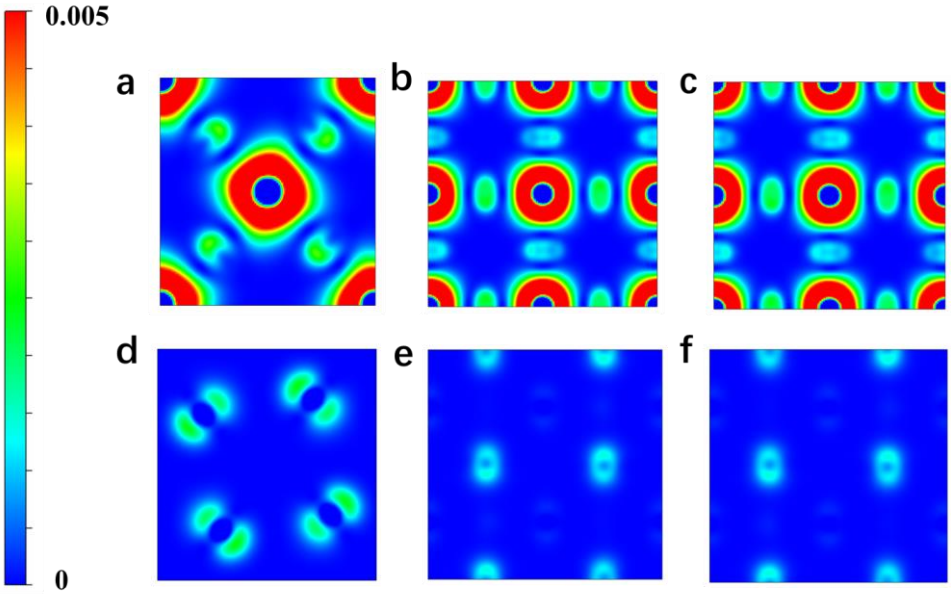

Figure S15. 2D electron density diagrams for sum of three degenerate CBM and two VBM respectively for $Cu(NH_3)_2PbI_3$. CBM charge density maps on the (010) (a), (101) (b), (10$\bar{1}$) (c) plane. VBM charge density maps on the (010) (d), (101) (e), (10$\bar{1}$) (f) plane.

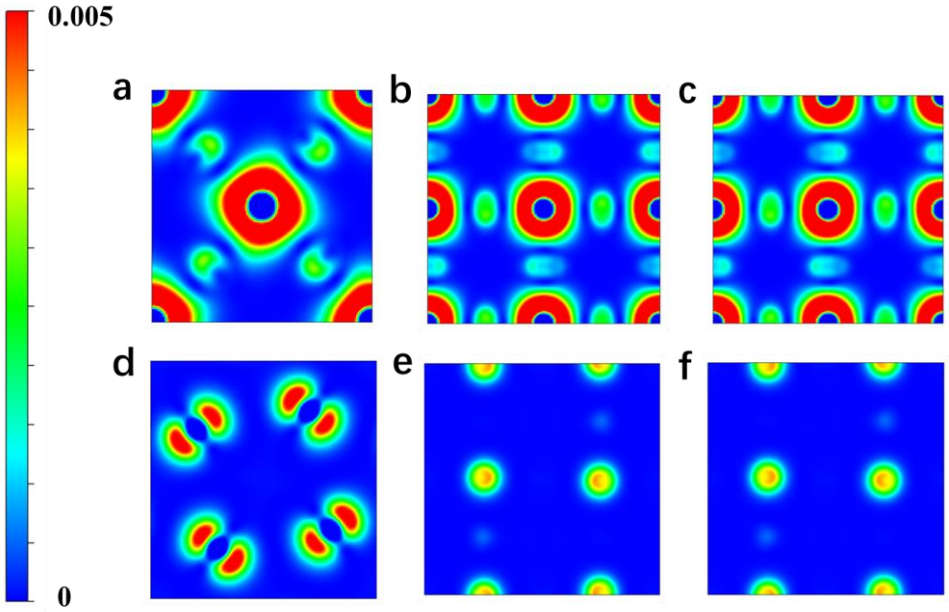

Figure S16. 2D Electron density diagrams for sum of three degenerate CBM and VBM respectively for $Ag(NH_3)_2PbI_3$. CBM charge density maps on the (010) (a), (101) (b), $(10\bar{1})$ (c) plane. VBM charge density maps on the (010) (d), (101) (e), $(10\bar{1})$ (f) plane.

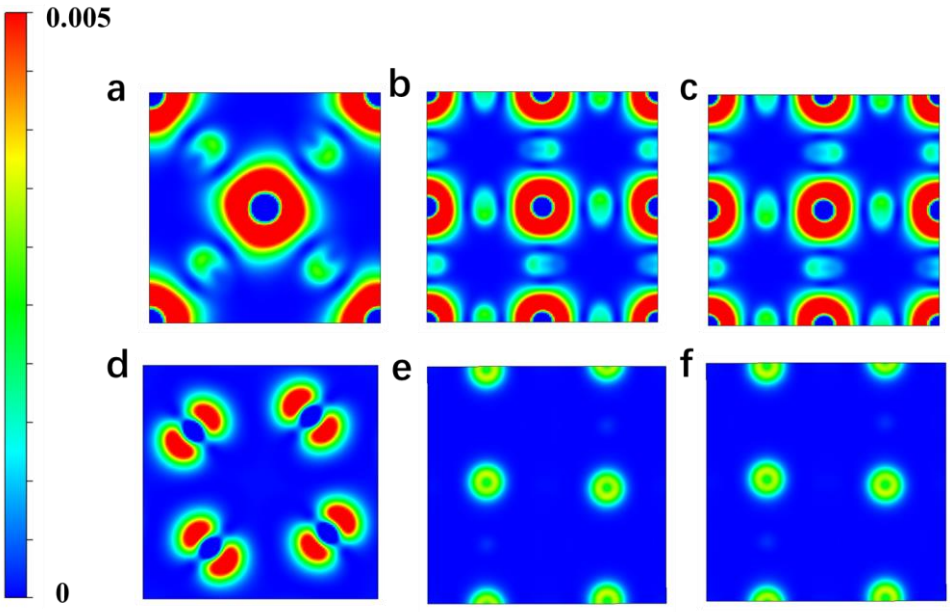

Figure S17. 2D electron density diagrams for sum of three degenerate CBM and VBM respectively for $Au(NH_3)_2PbI_3$. CBM charge density maps on the (010) (a), (101) (b), $(10\bar{1})$ (c) plane. VBM charge density maps on the (010) (d), (101) (e), $(10\bar{1})$ (f) plane.

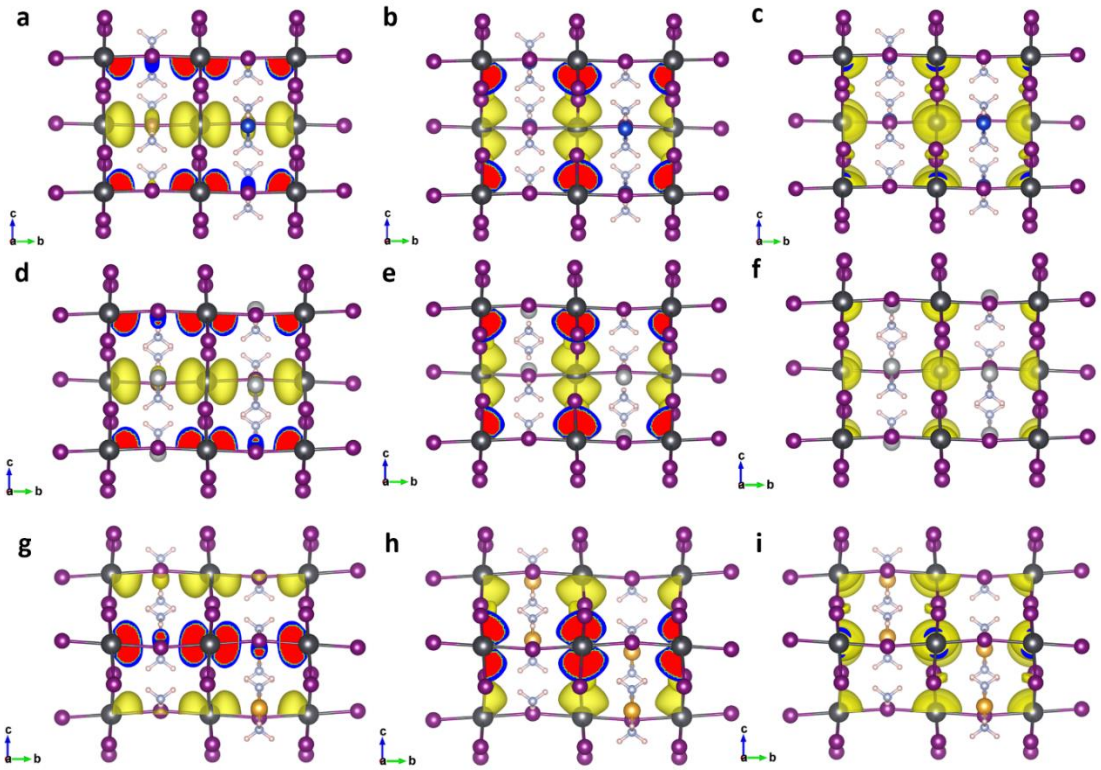

Figure S18. Isosurface plot of the self-consistent electron density (isovalue=0.0008 *e*/Bohr^3) of the degenerate conduction band minimum of $Cu(NH_3)_2PbI_3$ (a-c), $Ag(NH_3)_2PbI_3$ (d-f), $Au(NH_3)_2PbI_3$ (g-h).

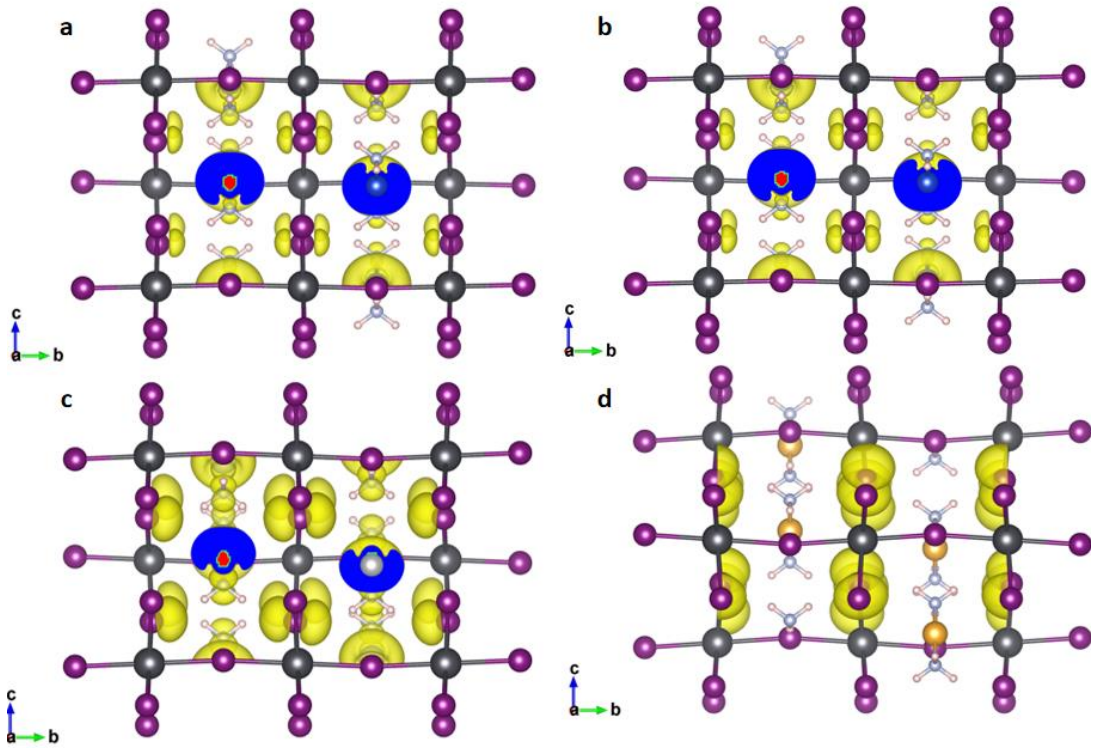

Figure S19. Isosurface plot of the self-consistent electron density (isovalue=0.0008 *e*/Bohr^3) of the valence band maximum of $Cu(NH_3)_2PbI_3$ (a-c), $Ag(NH_3)_2PbI_3$ (d-f), $Au(NH_3)_2PbI_3$ (g-h).

11. Brillouin zone high symmetry points

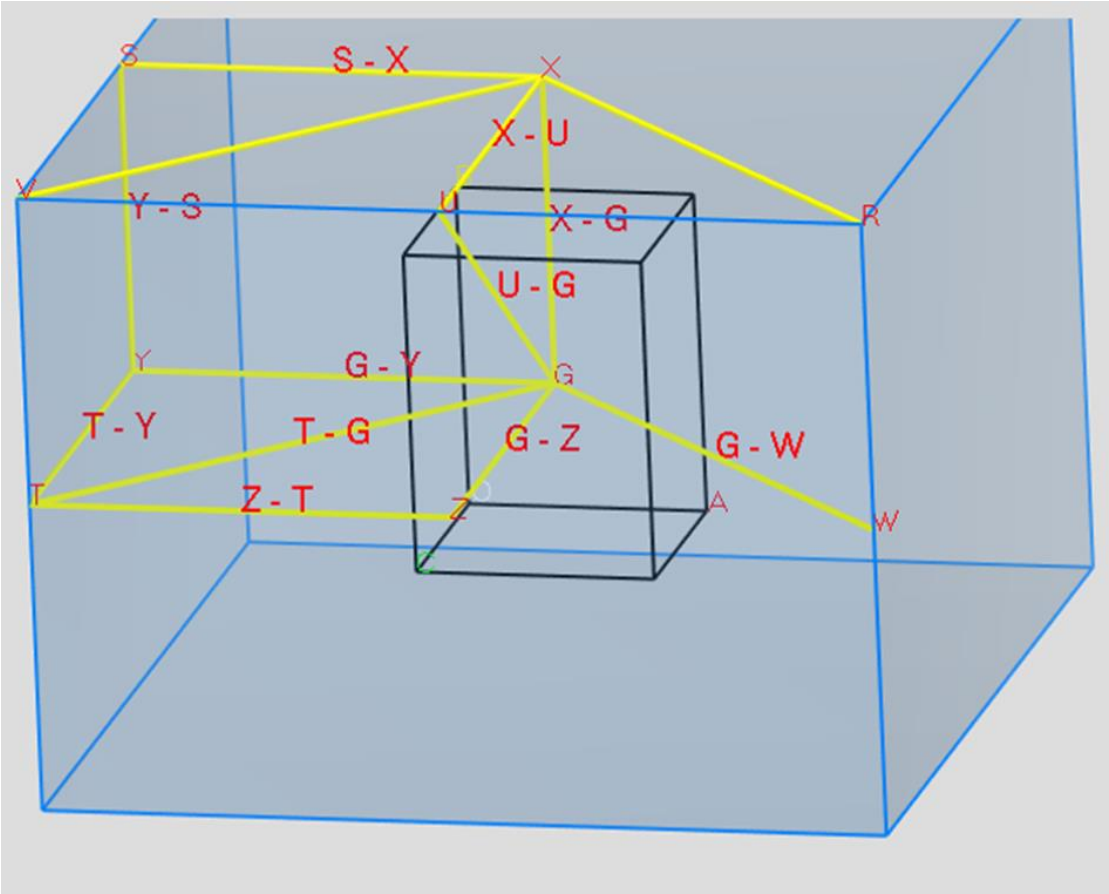

Figure S20. Brillouin zone high symmetry points in reciprocal space used in band structure calculations, Γ-X, Γ-T, Γ-W (Γ-X, Γ-Y, Γ-Z) are Pb-I skeleton (axis directions) directions of $Ag(NH_3)_2PbI_3$ and $Au(NH_3)_2PbI_3$ at CBM and VBM. Γ-X, Γ-T, Γ-W (Γ-X, Γ-Y, Γ-Z) are Pb-I skeleton (axis directions) directions of $Cu(NH_3)_2\,PbI_3$ at CBM. X-Γ, X-V, X-R (X-Γ, X-U, X-S) are Pb-I skeleton (axis directions) directions of $Cu(NH_3)_2\,PbI_3$ at VBM.

12. Electron and hole effective masses

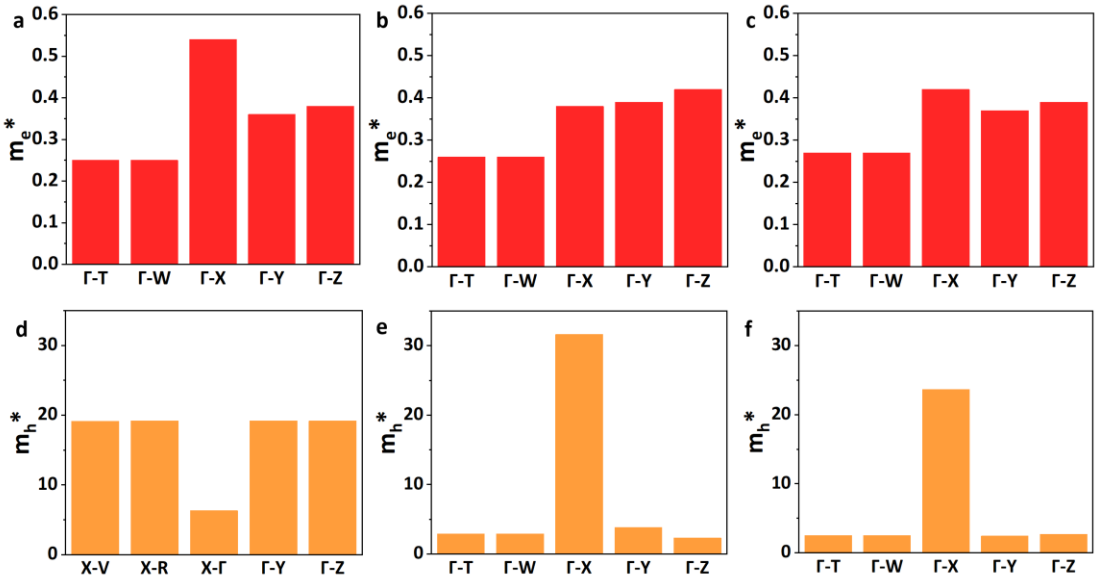

Figure S21. Minimal electron effective masses among degenerated CB (spin up) along the direction of the inorganic framework and axis of $Cu(NH_3)_2PbI_3$ (a), $Ag(NH_3)_2PbI_3$ (b), $Au(NH_3)_2PbI_3$ (c). Minimal hole effective masses among degenerated VB along the direction of the inorganic framework and axis of $Cu(NH_3)_2PbI_3$, (d) $Ag(NH_3)_2PbI_3$ (e), $Au(NH_3)_2PbI_3$ (f).

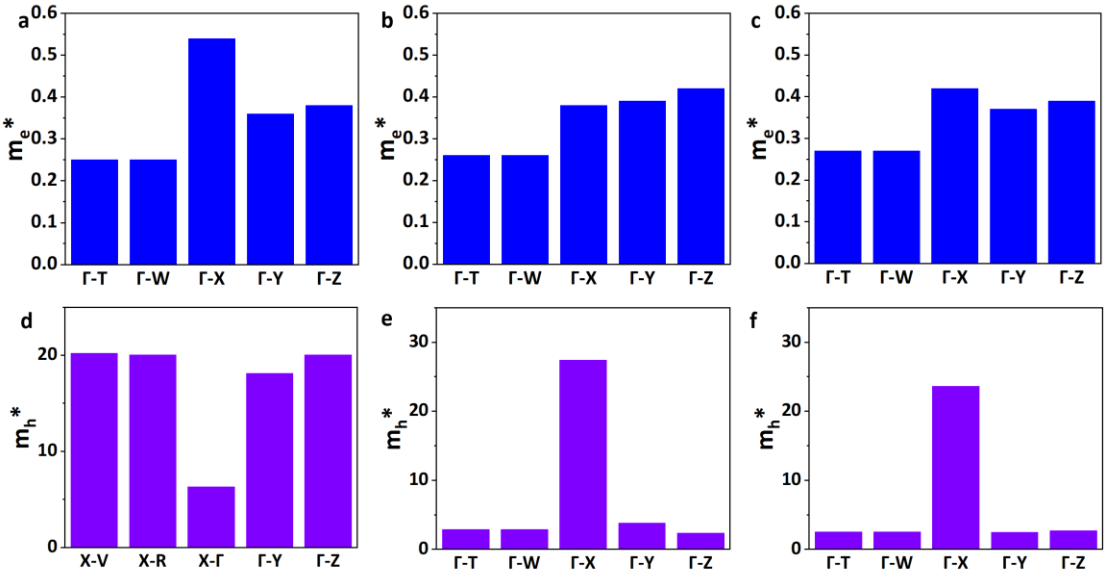

Figure S22. Minimal electron effective masses among degenerated CB (spin down) along the direction of the inorganic framework of $Cu(NH_3)_2PbI_3$ (a), $Ag(NH_3)_2PbI_3$ (b), $Au(NH_3)_2PbI_3$ (c).

Minimal hole effective masses among degenerated VB along the direction of the inorganic framework of $Cu(NH_3)_2PbI_3$, (d) $Ag(NH_3)_2PbI_3$ (e), $Au(NH_3)_2PbI_3$ (f).

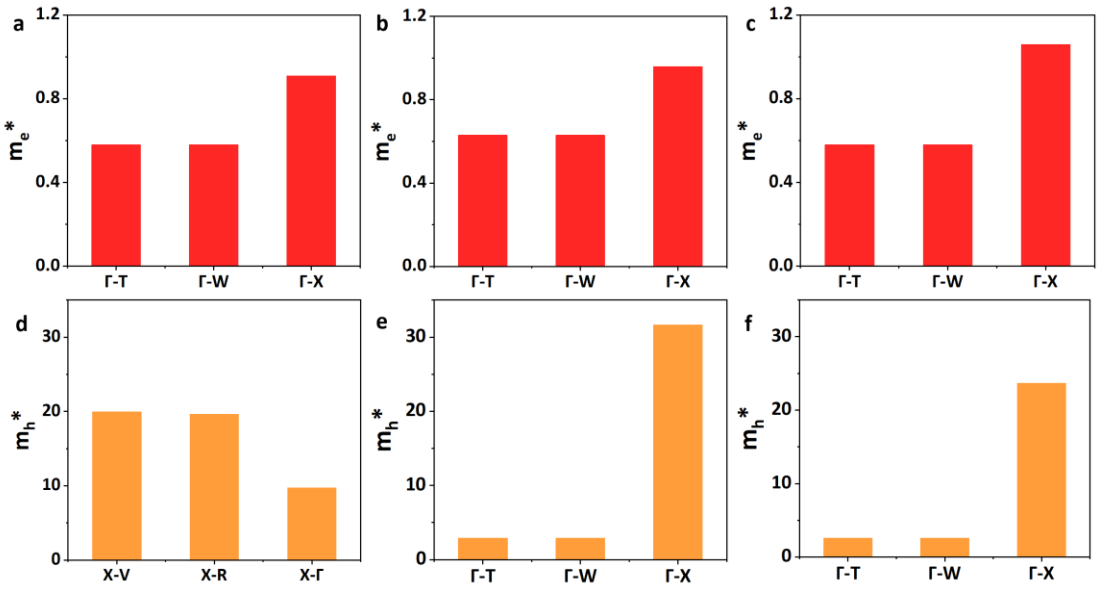

Figure S23. Harmonic mean of electron effective masses among degenerated CB (spin up) along the direction of the inorganic framework of $Cu(NH_3)_2PbI_3$ (a), $Ag(NH_3)_2PbI_3$ (b), $Au(NH_3)_2PbI_3$ (c). Harmonic mean of hole effective masses among degenerated VB (spin up) along the direction of the inorganic framework of $Cu(NH_3)_2PbI_3$, (d) $Ag(NH_3)_2PbI_3$ (e), $Au(NH_3)_2PbI_3$ (f).

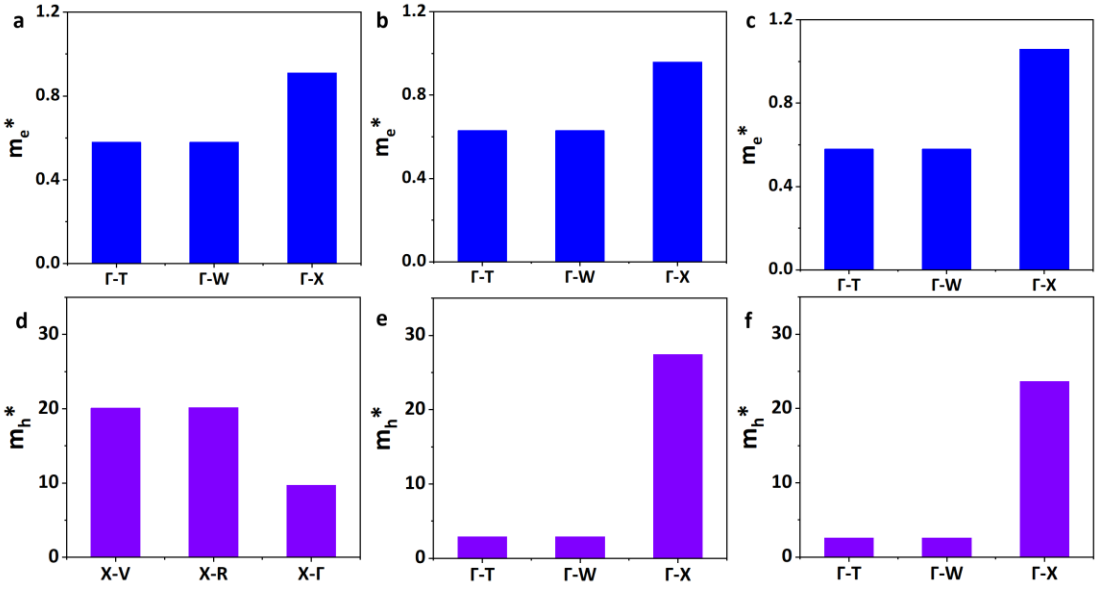

Figure S24. Harmonic mean of electron effective masses among degenerated CB (spin down) along the direction of the inorganic framework of $Cu(NH_3)_2PbI_3$ (a), $Ag(NH_3)_2PbI_3$ (b), $Au(NH_3)_2PbI_3$ (c).

Harmonic mean of hole effective masses among degenerated VB (spin down) along the direction of the inorganic framework of $Cu(NH_3)_2PbI_3$, (d) $Ag(NH_3)_2PbI_3$ (e), $Au(NH_3)_2PbI_3$ (f).

References

S1 G. Kresse and J. Hafner, *J. Phys.-Condes. Matter,* **1994**, 6, 8245-8257

S2 S. Lu, Q. Zhou, Y. Ouyang, Y. Guo, Q. Li and J. Wang, *Nat. Commun.,* **2018**, 9, 3405

S3 P.E. Blöchl, *Phys. Rev. B,* **1994**, 50, 17953-17979

S4 J.P. Perdew, A. Ruzsinszky, G.I. Csonka, O.A. Vydrov, G.E. Scuseria, L.A. Constantin, X. Zhou and K. Burke, *Phys. Rev. Lett.,* **2008**, 100, 136406

S5 E. Mosconi, P. Umari and F. De Angelis, *Phys. Chem. Chem. Phys.,* **2016**, 18, 27158-27164

S6 P. Umari, E. Mosconi and F. De Angelis, *Sci. Rep.,* **2014**, 4, 4467

S7 P. Giannozzi, S. Baroni, N. Bonini, M. Calandra, R. Car, C. Cavazzoni, D. Ceresoli, G.L. Chiarotti, M. Cococcioni, I. Dabo, A. Dal Corso, S. de Gironcoli, S. Fabris, G. Fratesi, R. Gebauer, U. Gerstmann, C. Gougoussis, A. Kokalj, M. Lazzeri, L. Martin-Samos, N. Marzari, F. Mauri, R. Mazzarello, S. Paolini, A. Pasquarello, L. Paulatto, C. Sbraccia, S. Scandolo, G. Sclauzero, A.P. Seitsonen, A. Smogunov, P. Umari and R.M. Wentzcovitch, *J. Phys.: Condens. Matter,* **2009**, 21, 395502

S8 P. Giannozzi, O. Andreussi, T. Brumme, O. Bunau, M. Buongiorno Nardelli, M. Calandra, R. Car, C. Cavazzoni, D. Ceresoli, M. Cococcioni, N. Colonna, I. Carnimeo, A. Dal Corso, S. de Gironcoli, P. Delugas, R.A. DiStasio, A. Ferretti, A. Floris, G. Fratesi, G. Fugallo, R. Gebauer, U. Gerstmann, F. Giustino, T. Gorni, J. Jia, M. Kawamura, H.Y. Ko, A. Kokalj, E. Küçükbenli, M. Lazzeri, M. Marsili, N. Marzari, F. Mauri, N.L. Nguyen, H.V. Nguyen, A. Otero-de-la-Roza, L. Paulatto, S. Poncé, D. Rocca, R. Sabatini, B. Santra, M. Schlipf, A.P. Seitsonen, A. Smogunov, I. Timrov, T. Thonhauser, P. Umari, N. Vast, X. Wu and S. Baroni, *J. Phys.: Condens. Matter,* **2017**, 29, 465901

S9 A. Togo, *J. Phys. Soc. Jpn.,* **2022**, 92, 012001

S10 A. Togo, L. Chaput, T. Tadano and I. Tanaka, *J. Phys.: Condens. Matter,* **2023**, 35, 353001

S11 V. Wang, N. Xu, J.-C. Liu, G. Tang and W.-T. Geng, *Computer Physics Communications,* **2021**, 267, 108033

S12 D. Shriver, M. Weller, T. Overton, F. Armstrong and J. Rourke, *Inorganic Chemistry*. Sixth ed.; Elsevier: 2014; Vol. 1, p 17.